

# Multifunctional Mesoporous Silica Nanoparticles Reinforced Silk Fibroin Composite with Antibacterial and Osteogenic Effects for Infectious Bone Rehabilitation

Dexiong Li<sup>1,\*</sup>, Jing Xie<sup>1,\*</sup>, Yubei Qiu<sup>1,2</sup>, Sihui Zhang<sup>1,3</sup>, Jiang Chen<sup>1,\*</sup>

<sup>1</sup>School and Hospital of Stomatology, Fujian Medical University, Fuzhou, People's Republic of China; <sup>2</sup>Fujian Key Laboratory of Fujian College and University, Fujian Medical University, Fuzhou, People's Republic of China; <sup>3</sup>Institute of Stomatology & Research Center of Dental and Craniofacial Implants, School and Hospital of Stomatology, Fujian Medical University, Fuzhou, People's Republic of China

\*These authors contributed equally to this work

Correspondence: Jiang Chen, School and Hospital of Stomatology, Fujian Medical University, Fuzhou, People's Republic of China, Tel +86 591 83735488, Fax +86 591 83700838, Email [jiangchen@fjmu.edu.cn](mailto:jiangchen@fjmu.edu.cn)

**Background:** Existing implant materials cannot meet the essential multifunctional requirements of repairing infected bone defects, such as antibacterial and osteogenesis abilities. A promising strategy to develop a versatile biomimicry composite of the natural bone structure may be accomplished by combining a multifunctional nanoparticle with an organic scaffold.

**Methods:** In this study, a quaternary ammonium silane-modified mesoporous silica containing nano silver (Ag@QHMS) was successfully synthesized and further combined with silk fibroin (SF) to fabricate the multifunctional nano-reinforced scaffold (SF-Ag@QHMS) using the freeze-drying method. Furthermore, the antibacterial and osteogenic effects of this composite were evaluated in vitro and in vivo.

**Results:** SF-Ag@QHMS inherited a three-dimensional porous structure (porosity rate:  $91.90 \pm 0.62\%$ ) and better mechanical characteristics ( $2.11 \pm 0.06$  kPa) than that of the SF scaffold (porosity rate:  $91.62 \pm 1.65\%$ ; mechanic strength:  $2.02 \pm 0.01$  kPa). Simultaneously, the introduction of versatile nanoparticles has provided the composite with additional antibacterial ability against *Porphyromonas gingivalis*, which can be maintained for 15 days. Furthermore, the expression of osteogenic-associated factors was up-regulated due to the silver ions eluting from the composite scaffold. The in vivo micro-CT and histological results indicated that the new bone formation was not only localized around the border of the defect but also arose more in the center with the support of the composite.

**Conclusion:** The multifunctional silver-loaded mesoporous silica enhanced the mechanical strength of the composite while also ensuring greater and sustained antibacterial and osteogenic properties, allowing the SF-Ag@QHMS composite to be used to repair infected bone defects.

**Keywords:** silk fibroin, quaternary ammonium silane, multifunctional, nano-reinforce, composite scaffold

## Introduction

Clinically, biofilm-related periodontitis or peri-implant inflammation often causes local infectious bone defects in dentistry, leading to tooth mobility and loss, implant failure and other repercussions.<sup>1</sup> Similar to other infectious diseases, bone infections require antibiotic treatment to eradicate infectious pathogens. However, antibiotics can hardly penetrate bone tissue, so oral antibiotic therapy cannot result in effective drug concentration.<sup>2</sup> Therefore, biocompatible anti-infective materials are often implanted as a supportive treatment nowadays.<sup>3</sup> It has been discovered that the most effective method for treating infectious bone defects is to prevent bacterial colonization, thus inhibiting the formation of biofilm on the surface of the implant material.<sup>4</sup> Therefore, a logical assumption is that constructing an efficient and continuously antibacterial implant material surface may be a better solution.

From the perspective of tissue engineering, bone tissue can be regarded as a complex nano-scale composite material—a lamellar structure formed by a mixture of organic extracellular matrix components, inorganic calcium phosphate nanoparticles and hydroxyapatite crystals.<sup>5</sup> Therefore, a biomimetic composite scaffold composed of the organic phase and inorganic components is considered an ideal substitute for bone reconstruction.<sup>6</sup> SF and chitosan (CS) are two kinds of organic matrices used to fabricate osteogenic scaffolds. SF, a natural biological macromolecule extracted from silkworm cocoons, is a potential material for scaffolds fabrication;<sup>7</sup> despite its many advantages, such as low price, easy availability, good biocompatibility and biodegradability and ease of processing into fiber.<sup>8–10</sup> However, neither antibacterial nor osteogenic bioactive activities were present in pure SF, which were fundamental requirements for infectious bone defect regeneration. CS is a biocompatible cationic degradable macromolecular polysaccharide with a certain antibacterial effect.<sup>11</sup> However, due to its fast degradation rate, low mechanical strength, and lack of elasticity and toughness, it was not suitable for use as a scaffold alone.<sup>12</sup> It has been found that the mixture of CS and SF solution can promote the formation of  $\beta$ -sheet, reduce the water solubility of SF and improve its mechanical properties.<sup>13</sup> Therefore, SF and CS are often used together to produce various biological scaffold materials.<sup>14,15</sup> Moreover, tyrosine, the main component of silk fibroin, has a potent electron-donating ability, possibly allowing it to combine with nanoparticles.<sup>16</sup>

To further improve the performance of SF-based materials, the introduction of multifunctional nanoparticles provides an efficient approach to achieving the required target properties for infectious bone regeneration.<sup>17</sup> However, many studies combine SF with different nanoparticles; they mainly focus on enhancing the mechanical and osteogenic properties of scaffolds while ignoring their versatility.<sup>18</sup> In our previous study, we successfully synthesized a multifunctional mesoporous silica nanoparticle containing nano silver (Ag@QHMS) with antibacterial properties and in vitro osteogenic induction capabilities.<sup>19,20</sup> However, due to their small size, nanoparticles cannot maintain enough support in defects. Simultaneously, they may enter veins or be endocytosed by cells, which may result in unfavorable reactions that restrict their direct application.<sup>21</sup> Therefore, the combination of the SF scaffold and Ag@QHMS mesoporous silica nanoparticles can more reasonably and effectively exert the biological activity of nanoparticles while also increasing the strength of the scaffold.

Overall, the purpose of this study was to examine the feasibility of producing a composite scaffold by mixing multifunctional Ag@QHMS nanoparticles with silk fibroin. In addition, antibacterial and osteogenic efficacy in vivo and in vitro were further evaluated to explore their potential clinical application prospects.

## Materials and Methods

### Materials

Tetraethyl orthosilicate (TEOS, AR), ammonium aqueous solution (25~28%), chitosan (CS, medium molecular) and cetyltrimethylammonium bromide (CTAB, AR) were purchased from Sigma-Aldrich (Shanghai, China). Carboalkylammonium chloride (SiQAC, purity 65%), silver nitrate ( $\text{AgNO}_3$ ), sodium citrate dehydrates, phosphate buffered saline (PBS), sodium bicarbonate ( $\text{Na}_2\text{CO}_3$ ) and ethanol were acquired from Xilong Scientific Cooperation (Beijing, China). Lithium bromide (LiBr) and glacial acetic acid (AR) were purchased from Aladdin (Shanghai, China). Silkworm cocoons were obtained from Huzhou, China.

### Synthesis of Nano-Reinforced Silk Fibroin Scaffold

The synthesis procedure is shown in Figure 1. At 60 °C, 20 g of silk degummed by  $\text{Na}_2\text{CO}_3$  solution was dissolved in 100 mL lithium bromide (9.3 mol/L) solution at 60°C, and after dialysis, centrifugation and filtration, 6 wt% SF stock solution was obtained. Next, at a volume ratio of 3:1, mix it with a CS solution (0.02 g/mL, pH = 7). The nano silver was then reduced from silver nitrate and coated layer by layer with silica shell by adding TEOS/ethanol (10 mM) under 24 h of constant severe agitation. In addition, a TEOS:SiQAC (9:1) mixture was added for covalent functionalization with quaternary ammonium salt (QAS). Under the protection of CTAB, the outer shell of silica can be etched into the mesoporous structure to synthesize the multifunctional nanoparticles of QAS-modified hollow mesoporous silica containing nano-Ag (Ag@QHMS). Under ultrasonic oscillation, the pure hollow mesoporous silica (HMS), QAS-modified

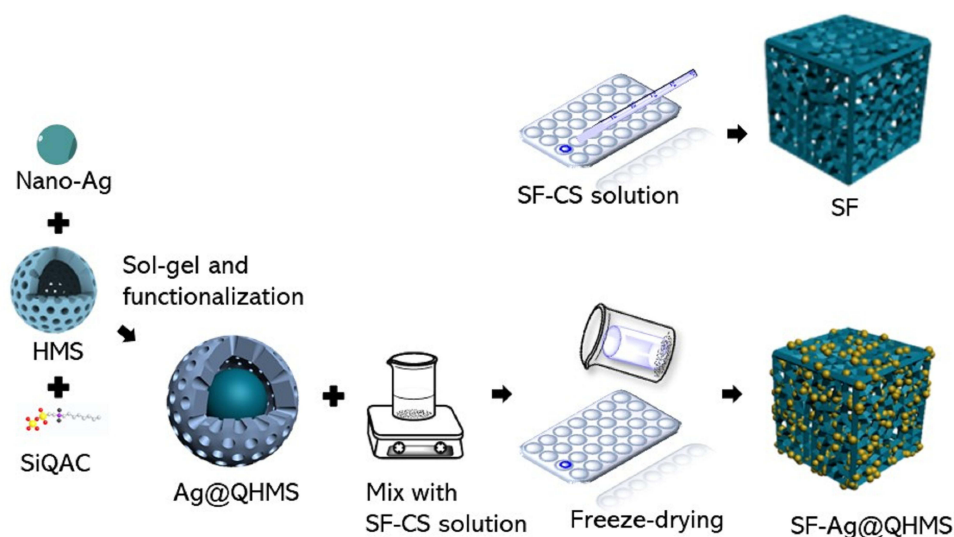


**Figure 1** Synthesis procedure of nano-reinforced scaffold composite.

hollow mesoporous silica (QHMS) and Ag@QHMS were added to the mixed solution at a biocompatibility concentration of 200  $\mu\text{g/mL}$ .<sup>18,19</sup> After removing the bubbles, an appropriate amount of crosslinking agent Genipin was added to strengthen the nano-reinforced crosslink for six hours. The mixtures were then added 1mL/well into a 24-well plate under ultrasonic variation, followed by a freeze-drying technique to obtain the composite scaffolds of SF-HMS, SF-QHMS and SF-Ag@QHMS. Pure SF served as a control.

## Scaffold Characterization

To investigate the structure of these nano-reinforced scaffolds, various characterization methods were utilized. A scanning electron microscope (SEM) was used to observe the surface features. The sample was observed at 100 kV using a JEM-2100 microscope (JEOL Co., Ltd., Tokyo, Japan). Furthermore, five areas of the SEM images were selected to measure the pore size. The X-ray diffraction (XRD) spectra were obtained using a Bruker D8 Discover powder diffractometer (Brook Scientific, Beijing, China) at a diffraction angle of  $20^\circ \leq 2\theta \leq 80^\circ$ . Fourier transform infrared (FTIR) spectra were measured under a Nicolet is50 (Thermo Fisher Scientific, Shanghai, China) to detect the peak shifts of the nanoparticles. A universal material testing machine (Shimadzu, China) was used to test the compressive strength of the scaffold in a wet state, and PBS was used as the soaking liquid. Prepare 10 mm high scaffold samples, load 100 N, load speed of 1 mm/min, load distance of 7 mm and measure five samples in each group. Draw a stress-strain curve, then draw a straight line parallel to the initial linear part from the 1% strain, and the ordinate of the intersection with the stress-strain curve is defined as the compressive strength.

## Scaffold Porosity, Swelling Rate and Hygroscopicity Rate

This experiment uses ethanol to examine the scaffold's porosity because, compared to the aqueous solution, ethanol solution is more easily able to permeate the tiny pores, resulting in a lower scaffold deformation rate and swelling rate. Each group took five samples for testing.

$$\text{Porosity rate(\%)} = \frac{V_1 - V_3}{V_2 - V_3} \times 100\%$$

where  $V_1$ :the volume after loading 10 mL of absolute ethanol is loaded into the graduated cylinder;

$V_2$ :the current volume of ethanol in the graduated cylinder after different sets of scaffolds of the same size are entirely immersed in the graduated cylinder;

$V_3$ :the amount of ethanol remaining after removing the scaffold volume.

$$\text{Swelling rate (\%)} = \frac{V_1 - V_0}{V_0} \times 100\%$$

$V_0$ :the initial volume of the scaffold;

$V_1$ :the wet volume of the scaffold after being immersed in PBS for 24 h.

$$\text{Hygroscopicity rate(\%)} = \frac{W_1 - W_2}{W_2} \times 100\%$$

$W_1$ :the weight of the scaffold after removing the surface water;

$W_2$ :the weight of the scaffold after completely drying in an oven at 65 °C.

### Contact Angle

SF, SF-HMS, SF-QHMS and SF-Ag@QHMS samples were placed on the platform, followed by adding ~3  $\mu\text{L}$  water each time to automatically measure the contact angle. Each sample was measured in parallel in the five different places to obtain the mean value.

### Ag Release Profile

The SF-Ag@QHMS scaffold was immersed in 200 mL simulated body fluid (SBF) and incubated for half a month at 37°C in a constant temperature shaker at 1000 rpm/min. At 2 h, 6 h, 12 h, 24 h, 2 days, 3 days, 7 days, 10 days, and 15 days, 2 mL of liquid was extracted, and the concentration of silver ions was measured using an inductively coupled plasma generator.

### Antibacterial Properties of the Scaffold

Using brain heart infusion broth containing 5 mg/L hemin, 1 mg/L vitamin K3 and 5% yeast extract (the solid plate needs to be supplemented with 2% agar and 5% defibrinated whole sheep blood at 50 °C), *Porphyromonas gingivalis* was cultured anaerobically at 37 °C, 80%  $\text{N}_2$ , 10%  $\text{H}_2$  and 10%  $\text{H}_2\text{O}$  (ATCC33277, American Type Culture Collection, USA) for 48 h. Adjust the bacterial suspension to  $3 \times 10^7$  colony forming units (CFU/mL) for use.

### Bacteria on the Scaffold

Place the sterilized SF, SF-HMS, SF-QHMS and SF-Ag@QHMS on the bottom of the 24-well plate, respectively. The bacterial suspensions prepared above were then appropriately inoculated on the surfaces of different materials and co-cultured in an anaerobic incubator for three days. After three days, the culture medium was removed, gently washed three times with PBS, and then fixed with 4% paraformaldehyde. Afterwards, the morphology and distribution of bacteria on different scaffolds were observed using SEM.

### Microbial Viability

For 15 days, inoculate SF, SF-HMS, SF-QHMS, and SF-Ag@QHMS with bacteria, respectively. At 1, 2, 3, 7, 10 and 15 days, an XTT reagent was added to evaluate the viability of residual bacteria on different scaffolds at 450 nm.

### In vitro Osteogenesis Effects

The cells used in the experiment were rat bone marrow mesenchymal stem cells (BMSC) purchased from the Chinese Academy of Sciences Cell Bank (Shanghai). The cells were recovered and incubated with low-sugar culture medium (containing 10% fetal serum, penicillin 100  $\mu\text{L}/\text{mL}$  and streptomycin 100  $\mu\text{g}/\text{mL}$ ) under 5%  $\text{CO}_2$  in a 37 °C cell incubator. When the cells have reached 80–90% confluency, add an appropriate amount of 0.25% trypsin for digestion and cell passage. The cells used in all experiments were ranged from P3 to P5.

### SEM Observation of Cell Morphology

Cell inoculation was the same as described above; After three days, the culture medium was removed, the cells were washed three times with PBS, and 4% paraformaldehyde was added to each well for 15 min at room temperature before being rinsed three times with PBS. The cells were then subjected to ethanol gradient dehydration, with concentrations of

30%, 50%, 70%, 80%, 90%, 95% and 100% for 10 min each. The use of CO<sub>2</sub> critical point drying, spray gold and scanning electron microscope to observe the morphology of the cells on scaffolds of different shapes.

### Cell Viability

The CCK-8 kit (Dojindo Laboratories, Shanghai, China) was used for cell viability detection. Place the scaffold in a 24-well plate and seed the cells with the same density as described above. Add 1 mL of complete culture medium to each well. On days one, three and five after seeding, 100  $\mu$ L of CCK-8 was added to each well. Incubate for 2 h at 37 °C, then aspirate 100  $\mu$ L from each well and transfer to a new 96-well plate, measure the absorbance (OD) at 450 nm with a microplate reader, and repeat the test three times for each group of scaffolds and each group of five samples.

### ALP Activity

An alkaline phosphatase activity (ALP) test and BCIP/NBT alkaline phosphatase staining were introduced to investigate the mineralization ability. In detail,  $2 \times 10^5$  BMSCs were first seeded onto each scaffold and co-culture for one week before being washed with PBS, and lysed with RIPA (Solarbio Science & Technology Co., Beijing, China) at 4 °C for 30 min, followed by centrifuging at 3000 rpm for 5 min to collect the supernatant. The amount of ALP in the supernatant was then evaluated at 405 nm using an alkaline phosphatase assay kit (Solarbio Science & Technology Co., Beijing, China). Meanwhile, a BCIP/NBT alkaline phosphatase color kit (Beyotime, Beijing, China) was introduced to access the distribution of ALP. The steps were as follows: the cells were washed twice with PBS and then fixed with 4.0% paraformaldehyde on ice for 30 min. The samples were rinsed three times again with PBS before being stained with 0.33% BCIP/0.66% NBT buffer for 10 min. The stained sample was observed and imaged using a microscope at 4x magnification.

### Osteogenic Differentiation-Related Gene Expression

The expression levels of osteogenic differentiation-related genes, including runt-related transcription factor 2 (Runx2), alkaline phosphatase (ALP), osteopontin (OPN), osteocalcin (OCN), bone sialoprotein (BSP) and collagen type 1 (Col-1), were further investigated by quantitative reverse transcription polymerase chain reaction (qRT-PCR). After two weeks, the total RNA of cells co-cultured on the scaffold was extracted using TRIzol (Takara Biomedical Technology Co., Ltd., Beijing, China), reverse transcript to the template using the PrimeScript™ RT reagent kit with gDNA Eraser (Takara Biomedical Technology Co., Ltd., Beijing, China), and then mixed with TB Green® Premix Ex Taq™ (Takara Biomedical Technology Co., Ltd., Beijing, China) for PCR on a LightCycler® 480 instrument (Roche Diagnostics Ltd., Shanghai, China). The primer sequences of the target genes are shown in Table 1. The resulting mRNA levels were normalized to GAPDH and compared with those of the control group using the  $2^{-\Delta\Delta Ct}$  method.

## In vivo Bone Formation Evaluation

### Establishment of Rat Jawbone Defects

All experimental procedures were approved by the Experimental Animal Ethics Committee of Fujian Medical University (No: FJMU-IACUC2019-0120) in accordance with the Guiding Principles for the Care and Use of Laboratory Animals (China).

**Table 1** The Primer Sequence

Target Gene Specific Primer Sequence (5' to 3')		
Gene	Forward Sequence	Reverse Sequence
<b>Runx2</b>	TCCCAGTATGAGAGTAGGTGTCC	GGCTCAGATAAGAGGGGTAAGAC
<b>ALP</b>	CCTAGACACAAGCACTCCCACTA	GTCAGTCAGGTTGTTCCGATTC
<b>Col</b>	TCTGACTGGAAGAGCGGAGAG	GAGTGGGGAACACACAGGTCT
<b>OCN</b>	GACCCTCTCTGCTCACTCTG	CACCTTACTGCCCTCCTGCTT
<b>BSP</b>	CGGCCACGCTACTTTCTTTA	CCCTCCTCCTCCGAACATATC
<b>GAPDH</b>	CGGCAAGTTCAACGGCACAGTCAAGG	ACGACATACTCAGCACCAGCATCACC

Thirty male SD rats (weighing about  $250 \pm 20$  g, provided by the Experimental Animal Center of Fujian Medical University, SYXK-2016-0006) were randomly divided into five groups: control, SF, SF-HMS, SF-QHMS and SF-Ag@QHMS. The surgical procedure was as follows: first, the rats were anaesthetized with sodium pentobarbital intraperitoneally. Next, a longitudinal incision of about 1.5 cm was made along the left mandible, 5 mm below the mandible, to expose the jaw area. A circular bone defect with a diameter of 3 mm under the anterior inferior outer oblique line of the first molar was created using a high-speed turbine and split drill. The prepared scaffolds were placed into the defect, and finally, the incisor was sutured.

### Micro-CT

All animals were sacrificed after six weeks, and the entire left mandible without any soft tissue was collected and fixed with 4% paraformaldehyde for 48 h. The regeneration of new bone in the defect was then measured using micro-CT. The N-Recon software was used to reconstruct the three-dimensional image of the bone defect area, and the CT-AN software was used for qualitative analysis, including bone volume in tissue volume (BV/TV), bone surface area to bone volume ratio (BS/BV), trabecular bone thickness (Tb.Th), trabecular bone number (Tb.N, 1/mm) and trabecular bone separation (Tb.Sp).

### Histopathology

After fixation, the harvested specimens were embedded in epoxy resin. All specimens were subsequently trimmed and polished to achieve a final thickness of 40  $\mu\text{m}$ . All slides were stained with HE and Masson tricolor, as previously described<sup>30</sup> and then observed and photographed under a light microscope (AxioCam ICc5; Carl Zeiss Microscopy GmbH, Munich, Germany).

### Statistics

Statistical analysis was performed using SPSS 22.0 (IBM Co., Chicago, IL, USA). The Shapiro–Wilk and Levene tests were performed to determine the normality and homogeneity of variance in each group of data. After that, each data group was analyzed by one-way analysis of variance and Bonferroni pairwise comparison. For all analyses, statistical significance was preset to  $\alpha = 0.05$ .

## Results

### Characterisation of Ag@QHMS Composite Scaffold

#### SEM Observation of Scaffold

The appearance of the scaffolds SF, SF-HMS, SF-QHMS and SF-Ag@QHMS are shown in Figure 2. Under a low magnification lens (800 $\times$ ), all four sets of scaffolds display a loose and irregular porous structure, with the pore walls appearing to stand up like leaves. However, under a medium magnification lens (2000 $\times$ ), the morphologies of these scaffolds are completely different. The pore wall of the pure SF scaffold was thin, and the surface texture was smooth. The hole walls of the SF-HMS, SF-QHMS and SF-Ag@QHMS were slightly thicker and denser. Under high magnification (10,000 $\times$ ), the hole walls were likely rough and scattered with spherical protrusions that were embedded in the hole wall. Furthermore, the nanoparticles in some areas have agglomeration. The pore size of each scaffold was  $217.35 \pm 36.48$   $\mu\text{m}$ ,  $167.73 \pm 42.79$   $\mu\text{m}$ ,  $152.57 \pm 35.12$   $\mu\text{m}$  and  $233.40 \pm 74.85$   $\mu\text{m}$ .

#### Fourier Transform Infrared Spectrum

The FTIR spectrum of the scaffolds is shown in Figure 3A. The peaks at  $\sim 1623$   $\text{cm}^{-1}$  and  $\sim 1518$   $\text{cm}^{-1}$  were due to C=O conjugate polarization and  $\text{NH}_2$  polarization, respectively. They represent the main characteristic functional groups of SF and CS, which are the main components of the scaffolds. The small peaks at  $\sim 460$   $\text{cm}^{-1}$  and  $\sim 1063$   $\text{cm}^{-1}$  resulted from the rocking motion and symmetrical stretching of Si-O-Si, respectively. These characteristic peaks of mesoporous silica appear on the three groups of scaffolds except SF, demonstrating the successful attachment of mesoporous silica nanoparticles.

#### X-Ray Diffraction

Figure 3B depicts the XRD spectra of SF, SF-HMS, SF-QHMS and SF-Ag@QHMS. The common small peaks at  $20.8^\circ$  and  $22.6^\circ$  were the  $\beta$ -sheets structure of silk fibroin. The diffraction of the mesoporous shell of silica contributed to the

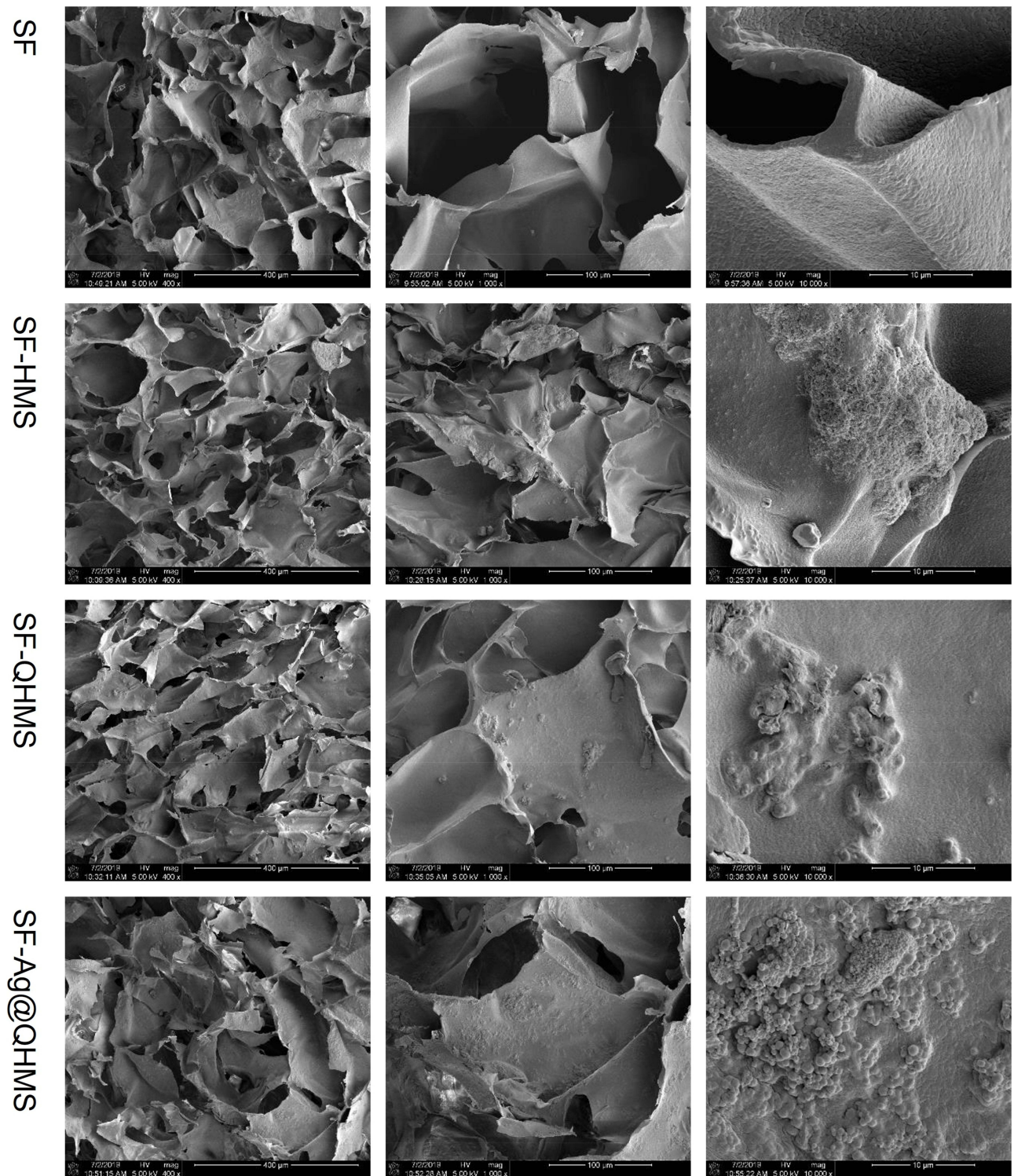


**Figure 2** SEM topography of SF, SF-HMS, SF-QHMS and SF-Ag@QHMS scaffolds (magnification: 800 $\times$ , 2000 $\times$  and 10,000 $\times$ ). All scaffolds exhibited a loose and irregular porous structure with a leaf-like pore wall. In more detail, the hole walls of the SF-HMS, SF-QHMS and SF-Ag@QHMS were slightly thicker and denser than pure SF. Nanoparticles can be seen as embedded in the wall, with agglomeration in some areas.

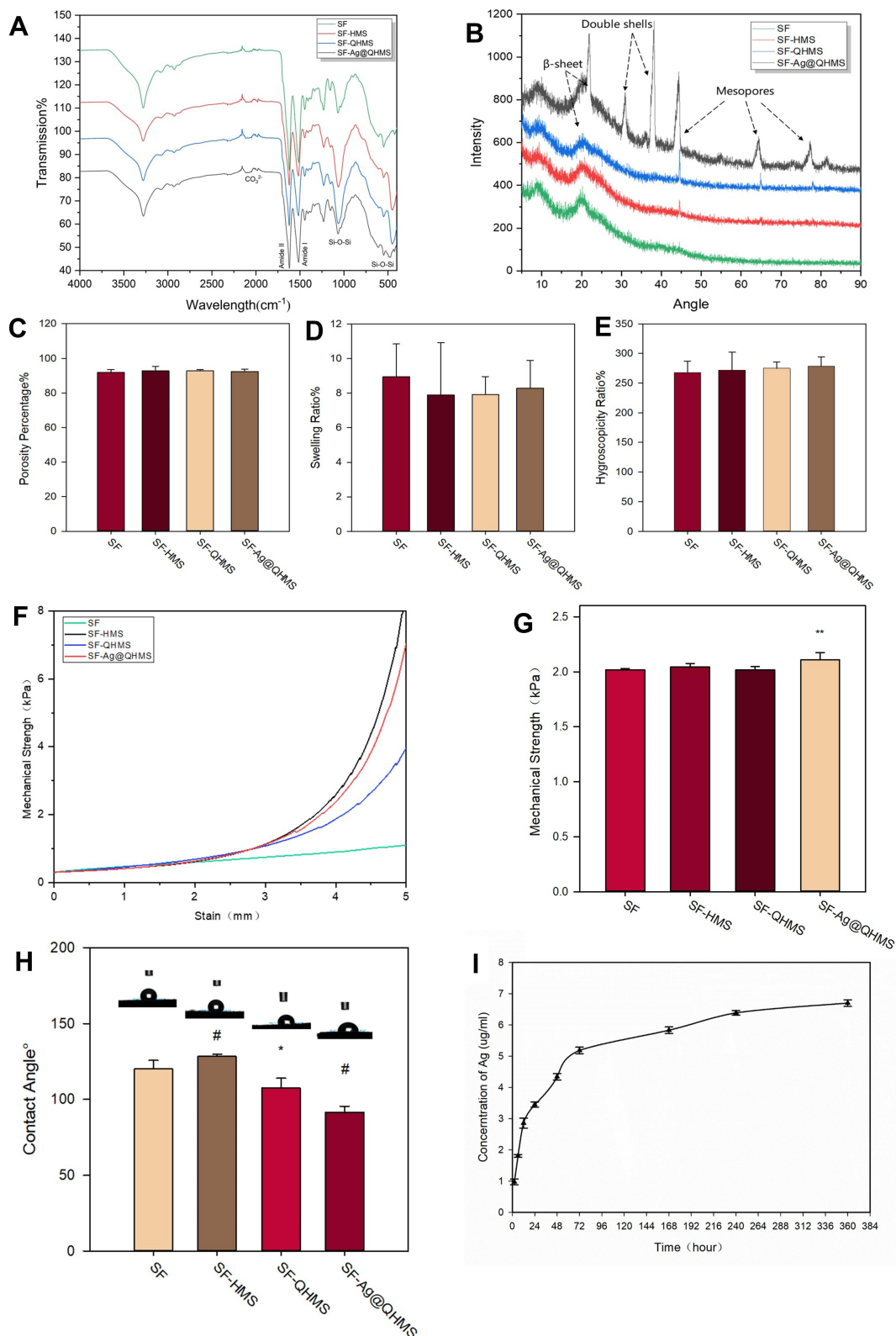


**Figure 3** Characterization of the scaffolds. (A) X-ray diffraction patterns; (B) Fourier transform infrared spectrum; (C) porosity percentage; (D) swelling rate; (E) hygroscopicity rate; (F) mechanical strength to stain of the scaffolds; (G) the statistical results of mechanical strength; (H) the static contact angle of the scaffolds. (N = 6, \* $p < 0.05$ ; \*\* $p < 0.01$ , # $p < 0.001$ ); (I) the release profile of Ag in SF-Ag@QHMS.

small peaks at 44.7°, 64.8° and 77.2° in SF-HMS, SF-QHMS and SF-Ag@QHMS. The diffraction peaks in SF-Ag@QHMS at 30.1° and 38.1° may be related to the double-layer mesoporous shell texture.

### Scaffold Porosity, Swelling Rate and Hygroscopicity Rate

As shown in Figures 3C–E, the porosity of SF, SF-HMS, SF-QHMS and SF-Ag@QHMS, which was necessary for nutrition and cell penetration, was  $91.62 \pm 1.65\%$ ,  $91.70 \pm 0.91\%$ ,  $91.98 \pm 0.62\%$  and  $91.90 \pm 0.62\%$ . The hygroscopicity rates for good biomaterials were  $267.9 \pm 19.0\%$ ,  $271.8 \pm 30.4\%$ ,  $274.9 \pm 10.5\%$  and  $278.3 \pm 16.1\%$ , respectively. The relative swelling rates were  $8.95 \pm 1.90\%$ ,  $7.88 \pm 3.04\%$ ,  $7.91 \pm 1.05\%$  and  $8.28 \pm 1.60\%$ , indicating the ability of space fit and support after compression. All of the above had no statistically significant difference ( $p > 0.05$ ).

### Mechanical Properties of the Scaffold

The mechanical strengths are shown in Figures 3F and G. The mechanical strengths of these scaffolds were  $2.02 \pm 0.01$  kPa,  $2.04 \pm 0.03$  kPa,  $2.01 \pm 0.03$  kPa and  $2.11 \pm 0.06$  kPa, respectively. It can be seen that the addition of different nanoparticles slightly enhanced the compressive strength of the scaffold. Among them, the difference between SF and SF-QHMS in compressive strength was statistically significant ( $p < 0.01$ ).

### Static Contact Angle

The contact angle reflects the surface energy and hydrophilicity of the surface of the biological material and the affinity of the biological material for proteins and other biological molecules. As shown in Figures 3H, the static contact angles of SF, SF-HMS, SF-QHMS and SF-Ag@QHMS were  $107.71 \pm 6.26^\circ$ ,  $91.57 \pm 3.92^\circ$ ,  $120.14 \pm 5.59^\circ$  and  $128.36 \pm 1.58^\circ$ , respectively. The addition of HMS to the SF scaffold resulted in the poorest hydrophilicity ( $p < 0.001$ ), while the addition of QHMS ( $p < 0.05$ ) and Ag@QHMS ( $p < 0.001$ ) increased the hydrophilicity of the scaffold.

### Ag Release Profile

Figure 3I shows the release of silver ions in SF-Ag@QHMS immersed in SBF, demonstrating that the overall release trend is slow and sustained for up to half a month. On the first day of soaking, Ag<sup>+</sup> released slightly quickly, reaching  $3.45 \mu\text{g/mL}$ , and then gradually reduced from days 2 to 15, with the highest release concentration not exceeding  $7 \mu\text{g/mL}$ .

## Antibacterial Test

### SEM Observation of Bacteria on the Scaffold

Figure 4A clearly illustrates the growth and distribution of bacteria on the surface of the scaffold, especially in the pores. The number and distribution of bacteria on SF-HMS were quite similar to SF, but the number of bacteria in SF-QHMS and the group was significantly reduced, and bacteria can merely see on SF-Ag@QHMS, showing scattered distribution.

### Bacteria Viability

The growth curves of bacteria on SF, SF-HMS, SF-QHMS and SF-Ag@QHMS within 15 days are shown in Figure 4B. The growth trend of bacteria in the SF and SF-HMS groups was common without pronounced inhibition. The bacteria proliferated rapidly within one to four days and then slowly over the next 15 days. Meanwhile, both SF-QHMS and SF-Ag@QHMS exhibited evident antibacterial effects within one to four days, but SF-QHMS gradually restored bacterial proliferation after four days, whereas SF-Ag@QHMS considerably inhibited bacterial proliferation for at least 15 days despite a weakening of its antibacterial effect.

## In vitro Osteogenesis Effects

### Cell Morphology of the Scaffolds

Figure 5A shows the morphology of BMSCs under SEM after three days of growth on four different scaffolds. It can be seen that the morphology of the cells was slightly different. On the SF, the cell body was plump, long and spindle-like, and some of the cells differentiated to form pseudopods attached to the surface of the scaffold. The cell body was expanded and the number of pseudopodia increased on SF-HMS. On the SF-QHMS and SF-Ag@QHMS, the differentiation of BMSCs was more pronounced. The cell body became wide and flat, and the cells were covered with many slender pseudopods, thereby increasing the cell adhesion ability.

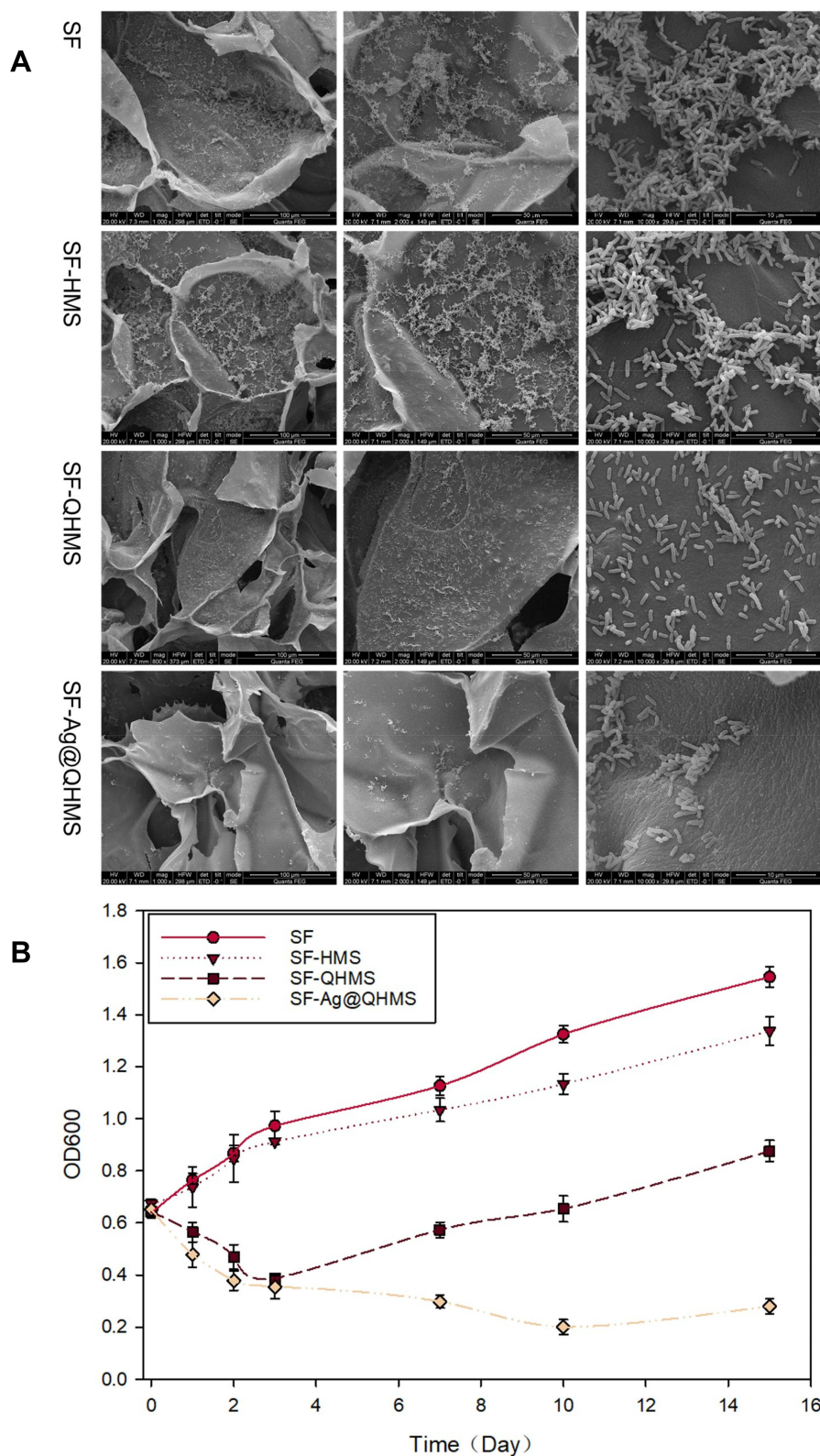


**Figure 4 (A)** Growth and distribution of bacteria on scaffolds after three days (magnification: 800×, 2000× and 10,000×); **(B)** the amounts of bacteria that remained in the medium depending on the time.

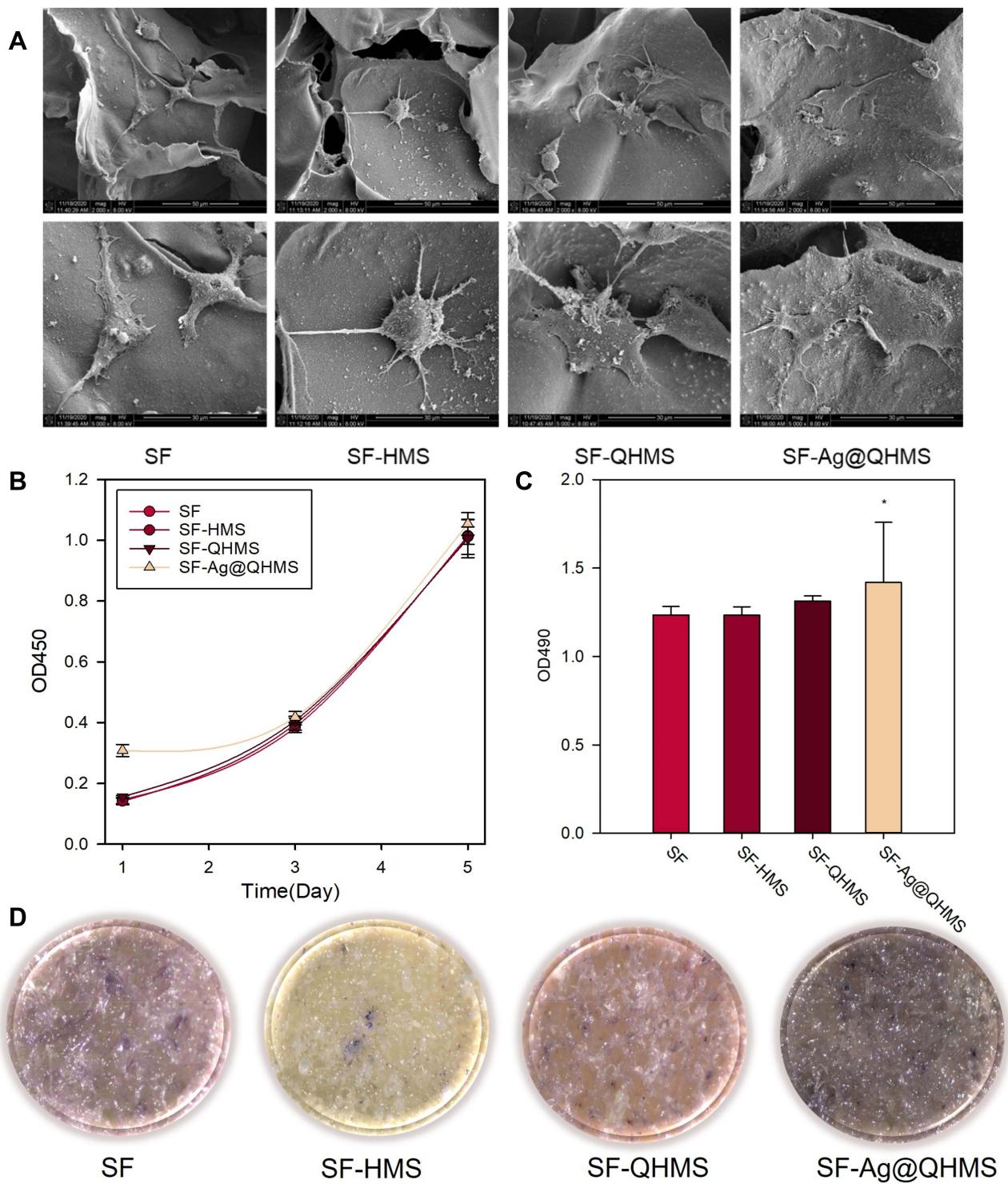


**Figure 5** (A) Cell morphology grown on scaffolds (Magnification: 2000 $\times$  and 5000 $\times$ ); (B) proliferation curve of BMSC on scaffolds; (C) ALP activity after one week of growth on scaffolds ( $*p < 0.05$ ); (D) the ALP distribution colored by BCIP/NBT.

### Cell Viability

The proliferation of BMSC on SF, SF-HMS, SF-QHMS and SF-Ag@QHMS is shown in Figure 5B. In general, SF, SF-HMS, SF-QHMS and SF-Ag@QHMS have similar effects on the proliferation of BMSCs, indicating that the addition of HMS, QHMS and Ag@QHMS did not affect SF scaffolds cytotoxicity. However, on the first day, it can be seen that the

proliferation of BMSCs in the SF-Ag@QHMS group was significantly higher than that of the other groups, indicating that the addition of nano silver in Ag@QHMS had a certain effect on promoting proliferation in the early stage.

### Quantitative Detection of ALP Activity

Figure 5C shows the quantitative analysis of ALP activity in the cell lysate seeded on the scaffold, in which only SF-Ag@QHMS significantly enhanced ALP activity compared to the others ( $p < 0.05$ ). As shown in Figure 5D, the alkaline phosphatase was scattered into the pores with blue-violet colouring on the scaffolds. Among them, the density and distribution in the SF-QHMS and SF-Ag@QHMS groups were more apparent. The density in the SF-HMS group was scattered and slightly less than in the SF group.

### Osteogenic Differentiation-Related Gene Expression

The gene expression levels after osteogenic induction on each scaffold for one week and two weeks are shown in Figure 6. It can be found that when SF-Ag@QHMS was compared to the control group, the expression levels of Runx2, OPN, OCN and BSP ( $p < 0.05$ ) in SF-Ag@QHMS increased at one week, and the up-regulating expression of ALP ( $p < 0.001$ ) and Col-1 ( $p < 0.001$ ) was more significant. However, SF-HMS and SF-QHMS only showed differences in up-regulating the expression of ALP (SF-HMS:  $p < 0.05$ , SF-QHMS:  $p < 0.01$ ). At two weeks, the Ag@QHMS continued to up-regulate the expression of the above genes, while the difference in ALP expression levels in SF-HMS and SF-QHMS at one week had returned to normal. The up-regulation of Col-1 in the SF-HMS group showed a significant difference ( $p < 0.05$ ), but it decreased the BSP expression ( $p < 0.05$ ).

## In vivo Assessment of the Bone Formation

### Micro-CT Imaging and Analysis

The bone defects prepared in the rat mandibular and the new bone formation six weeks after scaffold implantation were observed using micro-CT scanning, as shown in Figure 7A. The reconstruction model clearly exhibited that the hollow circle bone defects had become partial bone filling after six weeks of scaffold implantation. Detailed information on the new bone is shown in Figure 7B. The ratio of bone volume in tissue volume (BV/TV) in SF was slightly lower than in the control group, while the new bone volume of SF, SF-HMS, SF-QHMS and SF-Ag@QHMS gradually increased, but only the difference between SF and SF-Ag@QHMS, was significant ( $p < 0.05$ ). The ratio of surface area to bone volume (BS/BV) decreased steadily, indirectly indicating that the osteogenesis volume in the region gradually increased. Similarly, the increasing trend in each group was found in the average trabecular thickness (Tb.Th) and the number of trabecular bones (Tb.N). The trabecular separation degree (Tb.Sp) was gradually reduced, indicating that an increase in new bone formation leads to a decrease in the average width between trabecular bones.

### Histological results

Figure 8 shows the histological changes in the bone defects after six weeks of healing through HE and Masson staining. At 40× magnification, it can be clearly seen that the bone defects had been fulfilled with certain new trabecular bones depending on the different scaffold implantations. In detail, these new trabecular bones, which mainly formed as strips or bone islands, aligned quite differently from the radial arrangement of the surrounding normal tissues. In addition, the formation of new bones that were dyed red by HE and blue by Masson was mainly located on the edge of the defects and then eventually moved towards the center. SF-QHMS and SF-Ag@QHMS produced more new bone than SF and SF-HMS, particularly in the central region. At 100× magnification, a small amount of undegradable blue-violet star reticular scaffolds remained between the disorderly arranged new bone trabecula.

## Discussion

The enormous advancement of materials science has witnessed the rapid development and remarkable progress of tissue engineering. Generally, a single-component scaffold cannot provide all the prerequisites for efficient tissue regeneration. To overcome these inevitable drawbacks, combining nanomaterials with tissue engineering scaffolds is necessary to produce ideal scaffolds that mimic the structure of a natural extracellular matrix, thereby providing relevant biomechanical guidance and effective bioactive factors for biological regeneration.<sup>18–20</sup>

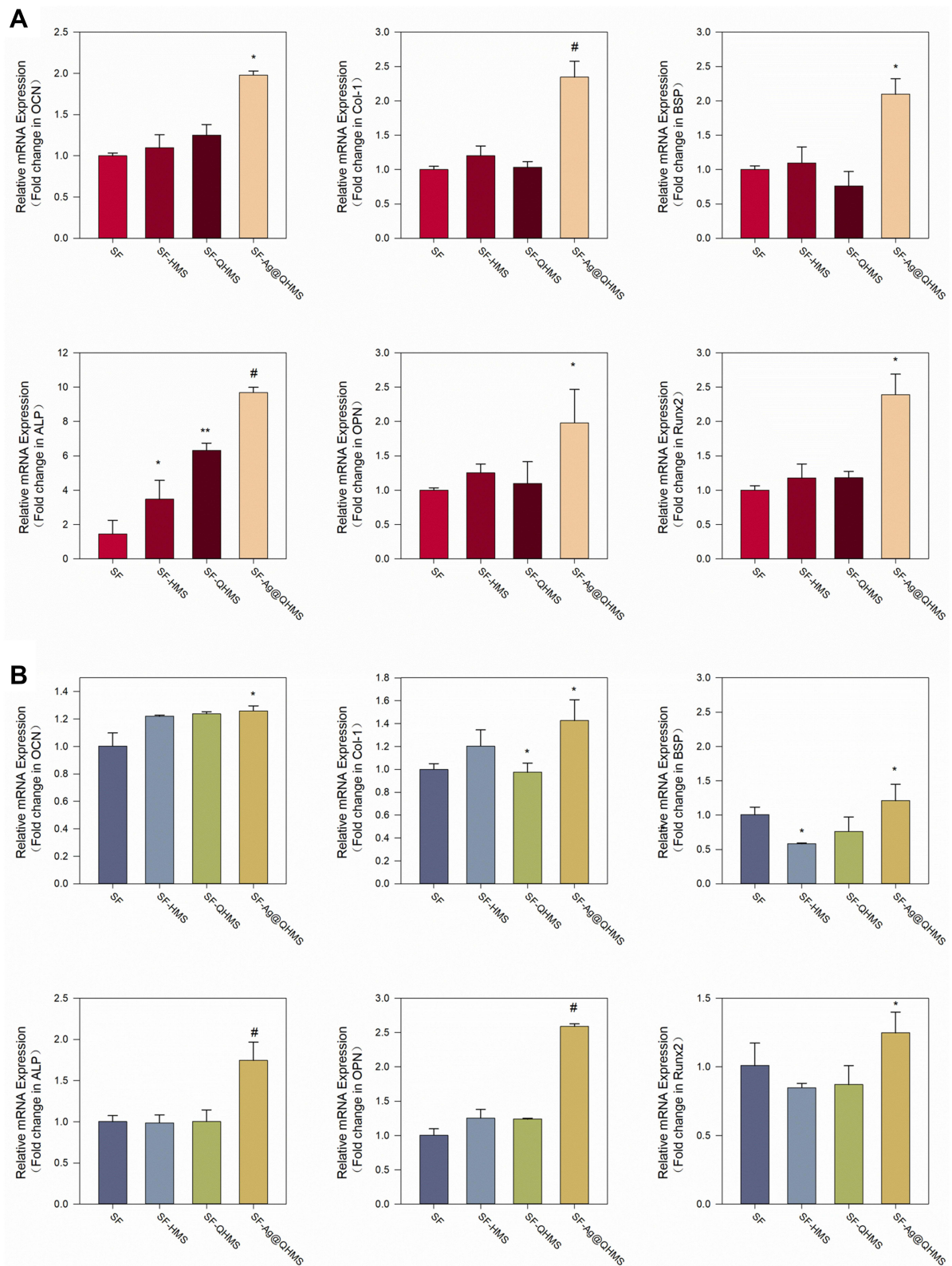


**Figure 6** Expression levels of genes related to osteogenic differentiation in BMSC after co-cultivation for one week (A) and two weeks (B). (\* $p < 0.05$ ; \*\* $p < 0.01$ ; # $p < 0.001$ ).

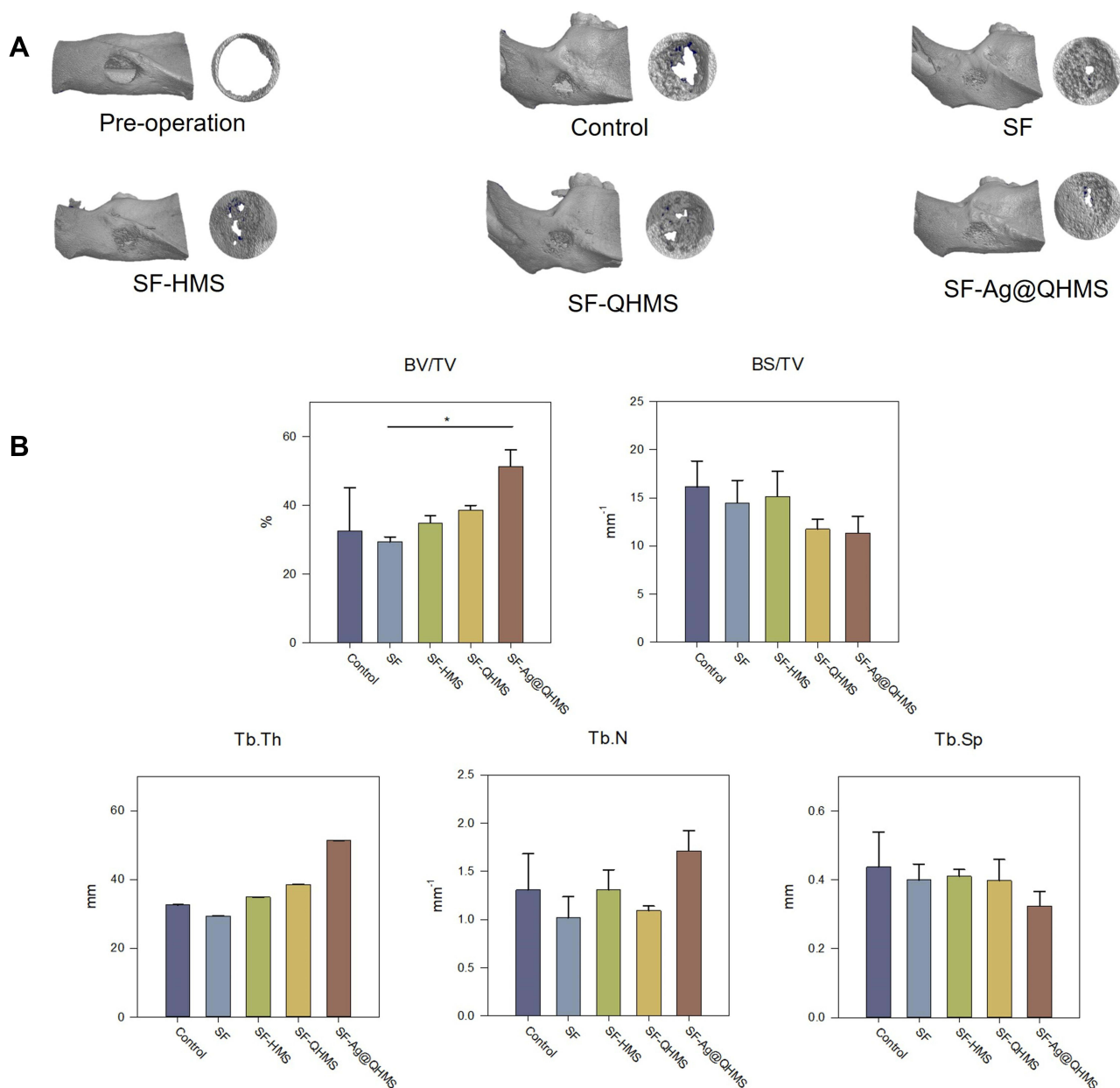


**Figure 7 (A)** Micro-CT three-dimensional reconstruction images of rat jaw defects before surgery and six weeks after scaffold implantation; **(B)** The evaluation of new bone formation in the bone defect area includes: the ratio of bone volume to the entire defect (BV/TV), the ratio of bone surface area to bone volume (BS/BV), trabecular bone thickness (Tb.Th) and bone size, the number of trabecular bones (Tb.N) and the separation of trabecular bones (Tb.Sp) (\* $p < 0.05$ ).

## Characterization of Ag@QHMS Composite Scaffold

The selection of scaffold matrix material influences not only cell adhesion, proliferation and differentiation but also affects the macroscopic tissue characteristics of the scaffold.<sup>22,23</sup> However, some studies have suggested that some adverse biological reactions, such as inflammation caused by natural silk, may be attributed to residual sericin.<sup>24</sup> Therefore, the scaffold matrix—SF with the same structure as natural type I collagen—was extracted using a high-temperature alkaline degumming procedure to resolve sericin.<sup>25</sup> The pores, which can promote better growth of cells, were directly produced by the freeze-drying method.<sup>26,27</sup> The pore size of SF-Ag@QHMS was  $233.40 \pm 74.85 \mu\text{m}$ ; among them, pores  $> 100 \mu\text{m}$  were conducive to the diffusion of oxygen and nutrients, resulting in cell survival and angiogenesis; pores of  $200\text{--}350 \mu\text{m}$  were particularly suitable for osteoblasts to grow into the scaffold.<sup>28</sup> At the same

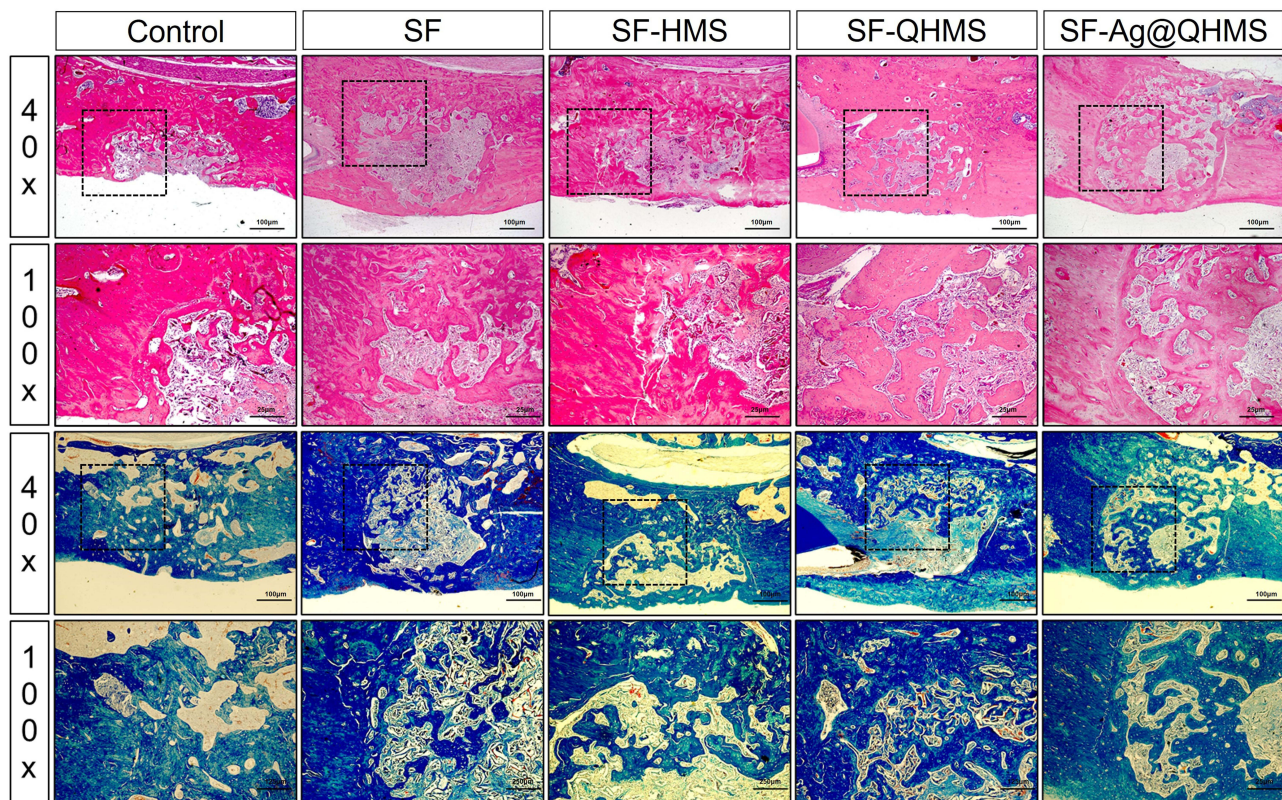


**Figure 8** HE and Masson staining of bone formation osteogenesis in different scaffolds after six weeks of healing.

time, the nanocomposite obtained by freeze-drying has a good bonding and crosslinking interface between the nanoparticles and the polymer matrix, which helps to increase the scaffold's strength.<sup>29</sup>

Mesoporous silica nanoparticles (MSN) lack the mechanical strength and proper space necessary for cell attachment, proliferation and differentiation, and new tissue formation, forcing MSN to combine with a certain three-dimensional scaffold.<sup>30</sup> Furthermore, the introduction of MSN can significantly strengthen the SF scaffold.<sup>31</sup> This may be due to the strong electrostatic interaction between the negatively charged tyrosine in SF and the positively charged QAS on Ag@QHMS.<sup>32</sup> However, different MSN may have a different effect on composite strength due to their own nanostructures. HMS and QHMS were hollow structures with lesser strength than the nearly solid Ag@QHMS core-shell structure.<sup>19,20</sup> Therefore, it is significant that only SF-Ag@QHMS strength increased. Interestingly, the inclusion of HMS, QHMS and Ag@QHMS nanoparticles thickened the pore wall without affecting the scaffold's hydrophobicity and swelling ability. The positive charge of QAS long chain and nano silver may contribute to the increase of hydrophilicity of SF-QHMS and SF-Ag@QHMS than that of SF. This effect, combined with an increased roughness of the nanoparticle surface, improved the scaffolds' ability to adsorb cells and protein macromolecules for osteogenic differentiation.<sup>33</sup>

The accumulating concentration of nano silver can be maintained at a sustained-release of 7 µg/mL for two weeks, which was regarded as safe for biological application.<sup>34</sup> The slow release of silver nanoparticles mainly depends on MSN, and the small 2–5 nm pore size of the mesoporous shell successfully controlled the release rate of silver, which has been confirmed in our published research. In this study, mesoporous nanoparticles anchored the surface of the SF scaffold, and its pores were practically covered by SF and CS. However, the degradation rate of SF and CS was fast, so the silver release curve was similar to that of Ag@QHMS.<sup>20</sup> The accumulated silver concentration mainly depends on the concentration of Ag@QHMS embedded in the composite.

## Antibacterial Activity of SF-Ag@QHMS

In addition to improving the physical and chemical properties of the scaffold, nanoparticles could be employed to supply biologically active components, providing the scaffold with more biologically active functionalities.<sup>15</sup> Because of the dual mode antibacterial effects of direct contact killing by the long QAS chain covalently bonding to the surface and slow-released antibacterial of nano silver, the long chain of surface-modified quaternary ammonium salt changes cell permeability, our synthesized Ag@QHMS nanoparticles have exhibited satisfactory antibacterial efficacy against *Escherichia coli*, *Staphylococcus aureus* and *Porphyromonas gingivalis*. The inclusion of nanoparticles to the SF-Ag@QHMS resulted in antibacterial activity. The antibacterial experiment showed that compared to the simple SF scaffold, the bacteria colonized on the surface of the SF-QHMS and SF-Ag@QHMS scaffolds were significantly lower. In addition, for at least four days, the antibacterial ability of SF-QHMS and SF-Ag@QHMS scaffolds remained highly effective due to the direct bacterial contact with the QAS modification surface. However, the antibacterial effects of SF-Ag@QHMS were reduced after four days, and the proliferation of bacteria was still significantly inhibited and maintained stably after 15 days. This is consistent with the release profile of silver ions. The continuing antibacterial activity from the initial stability helps the implanted scaffold resist forming plaque biofilm and better perform its osteogenic function.

## Osteogenesis Effect of SF-Ag@QHMS

SEM results showed that the surface of the pore wall of the nano-reinforced composite scaffold synthesized in this study was rougher, and the hydrophilicity increased after positively charged modification, which resulted in a slight alteration of the cell morphology. The nano-reinforced scaffold induced the cell body to become larger and pseudopodia accretion for better cell adhesion. Wang et al also found that the presence of MSN in the hydrogel enabled the composite hydrogel to absorb more protein and significantly improve cell adhesion.<sup>35</sup> Furthermore, it was challenging to improve cell proliferation and directed differentiation using a simple polymer or protein scaffold because of its limited biological activity.<sup>30</sup> MSN can be used as a reservoir of biologically active factors and combined with a scaffold to improve regeneration ability.<sup>36,37</sup> As our toxicity and proliferation results showed, SF and the other three nano-reinforced scaffolds generally have the same effect on the proliferation of BMSCs. Only SF-Ag@QHMS slightly promoted better proliferation on the first day, indicating that the biologically active function of the SF scaffold was enhanced by the Ag@QHMS nanoparticles. The possible reason may be that the Ag@QHMS nanoparticles could adaptively promote cell proliferation in a short period of time through the slow release of Ag<sup>+</sup>. At the same time, this low level of Ag<sup>+</sup> had certain osteogenic activity.<sup>38</sup> In addition, studies have pointed out that MSN particles have a certain proliferation effect on osteoblast precursors.<sup>39</sup> This nano-scale biological activity has also successfully endowed the SF scaffold with improved osteogenesis performance either in vivo or in vitro, such as the up-regulated expression of osteogenesis-related genes. In particular, the in vivo new bone formation induced on the scaffold demonstrated that under the support of the scaffold, osteoblasts above or below the scaffold could penetrate into the pores for growth, proliferation, differentiation and mineralization, allowing new bone to be generated from the center of the defects. In contrast, the new bone was first formed at the edge of the defect and gradually migrated towards the center in the control group. Therefore, nanoparticle-enhanced composite scaffolds may be a potential approach for the application of nanoparticles, such as MSN, in the field of tissue regeneration.

Nevertheless, it is important to note that the osteogenic effects of this multifunctional nanoparticle in vivo were not as good as those in vitro. This partly reflects the limitations of in vitro experiments. The conditions in vitro were more controllable and simpler, and the study period was usually only 7 to 21 days, during which the concentration of Ag<sup>+</sup> was relatively controlled without cytotoxicity. However, the composite scaffold was implanted into the defects for six weeks in vivo, which may have resulted in the accumulation of Ag<sup>+</sup> in the body and a disruption of the osteogenic effects. Therefore, the use of such composite scaffolds needs to be cautious and further improved.

## Conclusion

The nano-reinforced composite scaffold based on Ag@QHMS nanoparticles and SF was successfully assembled, inheriting the three-dimensional porous structure and better mechanical properties of the SF scaffold.

Simultaneously, the introduction of versatile nanoparticles has provided the composite with additional antibacterial ability against *Porphyromonas gingivalis*, which can be maintained for 15 days. Furthermore, the expression of osteogenic-associated factors was up-regulated due to the silver ion eluting from the composite scaffold. The in vivo osteogenesis results showed that the new bone formation was not only localized around the border of the defect but also arose more in the center with the support of the composite. In summary, the SF-Ag@QHMS composite scaffold has the dual functions of antibacterial and osteogenesis and allowing for its application in the treatment of infectious bone deformities.

## Data Sharing Statement

The data used to support the findings of this study are available from the corresponding author upon request.

## Acknowledgments

This work was mainly carried out in the Fujian Key Specialty Laboratory (20521189). The author is very grateful for the confocal microscopy observations by the Key Laboratory of Integrated Traditional Chinese and Western Medicine, Fujian University of Traditional Chinese Medicine, and the assistance provided by the instrument sharing platform of Fuzhou University for material performance characterization.

## Funding

This work was funded by Startup Fund for Scientific Research, Fujian Medical University (Grant number: 2021QH1134), and the Nature Science Foundation of Fujian Province (Grant number: 2022J01768).

## Disclosure

The authors declare no conflicts of interest.

## References

1. Kinane DF, Stathopoulou PG, Papapanou PN. Periodontal diseases. *Nat Rev Dis Primers*. 2017;3:17038. doi:10.1038/nrdp.2017.38
2. Budiati AS, Zainuddin M, Khotib J. Biocompatible composite as gentamicin delivery system for osteomyelitis and bone regeneration. *Int J Pharm Pharm Sci*. 2014;6(3):223–226.
3. Xu X, Gu Z, Chen X, et al. An injectable and thermosensitive hydrogel: promoting periodontal regeneration by controlled-release of aspirin and erythropoietin. *Acta Biomater*. 2019;86:235–246. doi:10.1016/j.actbio.2019.01.001
4. Zhang C, Zhu C, Yu G, et al. Management of infected bone defects of the lower extremities by three-stage induced membrane technique. *Med Sci Monit*. 2020;26:e919925. doi:10.12659/MSM.919925
5. He XT, Li X, Xia Y, et al. Building capacity for macrophage modulation and stem cell recruitment in high-stiffness hydrogels for complex periodontal regeneration: experimental studies in vitro and in rats. *Acta Biomater*. 2019;88:162–180. doi:10.1016/j.actbio.2019.02.004
6. Ebrahimi M, Botelho M, Lu W, et al. Synthesis and characterization of biomimetic bioceramic nanoparticles with optimized physicochemical properties for bone tissue engineering. *J Biomed Mater Res A*. 2019;107(8):1654–1666. doi:10.1002/jbm.a.36681
7. Patil PP, Reagan MR, Bohara RA. Silk fibroin and silk-based biomaterial derivatives for ideal wound dressings. *Int J Biol Macromol*. 2020;164:4613–4627. doi:10.1016/j.ijbiomac.2020.08.041
8. Holland C, Numata K, Rnjak-Kovacina J, et al. The biomedical use of silk: past, present, future. *Adv Healthc Mater*. 2019;8(1):e1800465. doi:10.1002/adhm.201800465
9. Gholipourmalekabadi M, Sapru S, Samadikuchaksaraei A, et al. Silk fibroin for skin injury repair: where do things stand? *Adv Drug Deliv Rev*. 2020;153:28–53. doi:10.1016/j.addr.2019.09.003
10. Farokhi M, Mottaghitlab F, Reis RL, Ramakrishna S, Kundu SC. Functionalized silk fibroin nanofibers as drug carriers: advantages and challenges. *J Control Release*. 2020;321:324–347. doi:10.1016/j.jconrel.2020.02.022
11. Yang H, Wang S, Bian H, et al. Extracellular matrix-mimicking nanofibrous chitosan microspheres as cell micro-ark for tissue engineering. *Carbohydr Polym*. 2022;292:119693. doi:10.1016/j.carbpol.2022.119693
12. Tao F, Cheng Y, Shi X, et al. Applications of chitin and chitosan nanofibers in bone regenerative engineering. *Carbohydr Polym*. 2020;230:115658. doi:10.1016/j.carbpol.2019.115658
13. Ran J, Hu J, Sun G, et al. A novel chitosan-tussah silk fibroin/nano-hydroxyapatite composite bone scaffold platform with tunable mechanical strength in a wide range. *Int J Biol Macromol*. 2016;93:87–97. doi:10.1016/j.ijbiomac.2016.08.062
14. Patel D, Dutta S, Hexiu J, et al. 3D-printable chitosan/silk fibroin/cellulose nanoparticle scaffolds for bone regeneration via M2 macrophage polarization. *Carbohydr Polym*. 2022;281:119077. doi:10.1016/j.carbpol.2021.119077
15. Torres P, Ribeiro N, Nunes C, et al. Toughening robocast chitosan/biphasic calcium phosphate composite scaffolds with silk fibroin: tuning printable inks and scaffold structure for bone regeneration. *Biomater Adv*. 2022;134:112690. doi:10.1016/j.msec.2022.112690
16. Fei X, Jia M, Du X, et al. Green synthesis of silk fibroin-silver nanoparticle composites with effective antibacterial and biofilm-disrupting properties. *Biomacromole*. 2013;14(12):4483–4488. doi:10.1021/bm4014149

17. Xu Z, Shi L, Yang M, et al. Preparation and biomedical applications of silk fibroin-nanoparticles composites with enhanced properties - A review. *Mater Sci Eng C Mater Biol Appl.* 2019;95:302–311. doi:10.1016/j.msec.2018.11.010
18. Cheng Y, Cheng G, Xie C, et al. Biomimetic silk fibroin hydrogels strengthened by silica nanoparticles distributed nanofibers facilitate bone repair. *Adv Healthc Mater.* 2021;10(9):e2001646. doi:10.1002/adhm.202001646
19. Bai YM, Mao J, Li DX, et al. Bimodal antibacterial system based on quaternary ammonium silane-coupled core-shell hollow mesoporous silica. *Acta Biomater.* 2019;85:229–240. doi:10.1016/j.actbio.2018.12.037
20. Li D, Qiu Y, Zhang S, et al. A multifunctional antibacterial and osteogenic nanomedicine: QAS-modified core-shell mesoporous silica containing Ag nanoparticles. *Biomed Res Int.* 2020;19(2020):4567049.
21. Ghaferi M, Raza A, Al Harthi S, et al. Mesoporous silica nanoparticles: synthesis methods and their therapeutic use-recent advances. *J Drug Target.* 2021;29(2):131–154. doi:10.1080/1061186X.2020.1812614
22. Cheng G, Dai J, Dai J, et al. Extracellular matrix imitation utilizing nanofibers-embedded biomimetic scaffolds for facilitating cartilage regeneration. *Chem Eng J.* 2021;410(2):128379. doi:10.1016/j.cej.2020.128379
23. Cheng G, Yin C, Tu H, et al. Controlled co-delivery of growth factors through layer-by-layer assembly of core-shell nanofibers for improving bone regeneration. *ACS Nano.* 2019;13(6):6372–6382. doi:10.1021/acsnano.8b06032
24. Gomes S, Leonor IB, Mano JF, et al. *Silk-Based Biomaterials.* Wiley-VCH Verlag GmbH & Co. KGaA; 2012.
25. Rockwood DN, Preda RC, Yucel T, et al. Materials fabrication from Bombyx mori silk fibroin. *Nat Protoc.* 2011;6(10):1612–1631. doi:10.1038/nprot.2011.379
26. Rezaei F, Sharifianjazi F, Esmailkhanian A, et al. Chitosan films and scaffolds for regenerative medicine applications: a review. *Carbohydr Polym.* 2021;273:118631. doi:10.1016/j.carbpol.2021.118631
27. Divakar P, Yin K. Anisotropic freeze-cast collagen scaffolds for tissue regeneration: how processing conditions affect structure and properties in the dry and fully hydrated states. *J Mech Behav Biomed.* 2019;90:350–364.
28. Bose S, Roy M, Bandyopadhyay A. Recent advances in bone tissue engineering scaffolds. *Trends Biotechnol.* 2012;30(10):546–554. doi:10.1016/j.tibtech.2012.07.005
29. Pourhaghgouy M, Zamanian A, Shahrezaee M, et al. Physicochemical properties and bioactivity of freeze-cast chitosan nanocomposite scaffolds reinforced with bioactive glass. *Mat Sci Eng C Mater.* 2016;58:180–186. doi:10.1016/j.msec.2015.07.065
30. Chen L, Zhou X, He C. Mesoporous silica nanoparticles for tissue-engineering applications. *Wiley Interdiscip Rev Nanomed Nanobiotechnol.* 2019;11(6):e1573. doi:10.1002/wnan.1573
31. Xin T, Gu Y, Cheng R, et al. Inorganic strengthened hydrogel membrane as regenerative periosteum. *ACS Appl Mater Inter.* 2017;9(47):41168–41180. doi:10.1021/acsmi.7b13167
32. Rose S, PrevotEAU A, Elziere P, et al. Nanoparticle solutions as adhesives for gels and biological tissues. *Nature.* 2014;505(7483):382–385. doi:10.1038/nature12806
33. Ganesh N, Ashokan A, Rajeshkannan R, et al. Magnetic Resonance Functional nano-hydroxyapatite incorporated poly (Caprolactone) composite scaffolds for in situ monitoring of bone tissue regeneration by MRI. *Tissue Eng Pt A.* 2014;20(19–20):2783–2794. doi:10.1089/ten.tea.2014.0161
34. Yuan Y, Ding L, Chen Y, et al. Nano-silver functionalized polysaccharides as a platform for wound dressings: a review. *Int J Biol Macromol.* 2022;194:644–653. doi:10.1016/j.ijbiomac.2021.11.108
35. Wang N, Ma M, Luo Y, et al. Mesoporous silica nanoparticles-reinforced hydrogel scaffold together with pinacidil loading to improve stem cell adhesion. *Chem Nano Mat.* 2018;4(7):631–641.
36. Hoang Thi TT, Cao VD, Nguyen TNQ, et al. Functionalized mesoporous silica nanoparticles and biomedical applications. *Mater Sci Eng C-Mater.* 2019;99:631–656. doi:10.1016/j.msec.2019.01.129
37. Zhang Q, Qin M, Zhou X, et al. Porous nanofibrous scaffold incorporated with S1P loaded mesoporous silica nanoparticles and BMP-2 encapsulated PLGA microspheres for enhancing angiogenesis and osteogenesis. *J Mater Chem B.* 2018;6(42):6731–6743. doi:10.1039/C8TB02138D
38. Li D, Li Y, Shrestha A, et al. Effects of programmed local delivery from a micro/nano-hierarchical surface on titanium implant on infection clearance and osteogenic induction in an infected bone defect. *Adv Healthc Mater.* 2019;8(11):e1900002. doi:10.1002/adhm.201900002
39. Beck GR Jr, Ha SW, Camalier CE, et al. Bioactive silica-based nanoparticles stimulate bone-forming osteoblasts, suppress bone-resorbing osteoclasts and enhance bone mineral density in vivo. *Nanomedicine.* 2012;8(6):793–803. doi:10.1016/j.nano.2011.11.003

International Journal of Nanomedicine

Dovepress

Publish your work in this journal

The International Journal of Nanomedicine is an international, peer-reviewed journal focusing on the application of nanotechnology in diagnostics, therapeutics, and drug delivery systems throughout the biomedical field. This journal is indexed on PubMed Central, MedLine, CAS, SciSearch®, Current Contents®/Clinical Medicine, Journal Citation Reports/Science Edition, EMBase, Scopus and the Elsevier Bibliographic databases. The manuscript management system is completely online and includes a very quick and fair peer-review system, which is all easy to use. Visit <http://www.dovepress.com/testimonials.php> to read real quotes from published authors.

Submit your manuscript here: <https://www.dovepress.com/international-journal-of-nanomedicine-journal>